Drift Wave Turbulence

W. Horton, J.-H. Kim, E. Asp, T. Hoang, T.-H. Watanabe, and H. Sugama

Citation: AIP Conference Proceedings **1013**, 1 (2008); doi: 10.1063/1.2939032
View online: http://dx.doi.org/10.1063/1.2939032
View Table of Contents: http://scitation.aip.org/content/aip/proceeding/aipcp/1013?ver=pdfcov
Published by the AIP Publishing

Drift Wave Turbulence

W. Horton*, J.-H. Kim*, E. Asp†, T. Hoang**, T.-H. Watanabe‡ and H. Sugama‡

*Institute for Fusion Studies, the University of Texas at Austin, USA
†Ecole Polytechnique Fédérale de Lausanne, Centre de Recherches en Physique des Plasmas Association Euratom-Confédération Suisse, CH-1015 Lausanne, Switzerland
**Assoc. Euratom-CEA, CEA/DSM/DRFC Cadarache, 13108 St Paul-Lez-Durance, France
‡National Institute for Fusion Science/Graduate University for Advanced Studies, Japan

Abstract. Drift waves occur universally in magnetized plasmas producing the dominant mechanism for transport of particles, energy and momentum across magnetic field lines. A wealth of information obtained from laboratory experiments for plasma confinement is reviewed for drift waves driven unstable by density gradients, temperature gradients and trapped particle effects. The modern understanding of origin of the scaling laws for Bohm and gyro-Bohm transport fluxes is discussed. The role of sheared flows and magnetic shear in reducing the transport fluxes is discussed and illustrated with large scale computer simulations. Plasmas turbulence models are derived with reduced magnetized fluid descriptions. The types of theoretical descriptions reviewed include weak turbulence theory and anisotropic Kolmogorov-like spectral indices, and the mixing length. A number of standard turbulent diffusivity formulas are given for the various space-time scales of the drift-wave turbulent mixing.

Keywords: Drift-waves, ITG, TEM, turbulence, transport, vortices, tokamaks
PACS: 52.35.Kt, 52.25.Fi, 52.25.Gj, 52.55.Fa, 52.35.Py

1. DRIFT WAVE MECHANISM

One of the most intellectually interesting problems in plasma physics is the problem of turbulence and the associated transport of the plasma properties including density, temperature and momentum. Plasma turbulence can be rather different from that in neutral fluids due to the numerous waves in the plasma. Plasma turbulence is closer to that of geostrophic flows on rotating planets where the Rossby wave is closely analogous to the plasma drift wave. At finite amplitude the wave dispersion often balances the wave nonlinearity to form solitary structures and coherent vortex structures. This aspect of plasma turbulence has been the topic of workshops and conferences both at ITP Santa Barbara [1] and the Marseille Workshops published as Benkadda et al. [2]. A monograph largely devoted to these problems is Horton and Ichikawa [3]. Drift waves are the most widely studied form of plasma turbulence in magnetized, confined plasmas so this first Chapter of the ITER School Proceedings is devoted to the study of these drift waves.

The search for controlled thermonuclear fusion has been dominated by the use of strong magnetic fields to confine laboratory plasmas. Through the 1970s to the 1990s the dominant thought was that the low-amplitude drift-wave turbulence would not seriously impede reaching the critical Lawson condition in MHD stable machines and sufficient auxiliary (external) plasma heating, $P_{\rm aux}$. Exceeding the Lawson condition, $n_e\tau_E \sim 1.5\times 10^{20}\,{\rm m}^{-3}{\rm s}$ at $25\,{\rm KeV}$, is required for D-T ignition. In the Lawson condition on $n_e\tau_E$, $\tau_E = W/(P_{\rm in} - dW/dt)$ is the energy confinement time defined by stored plasma energy (W), the power input ($P_{\rm in}$) and the time variation of the stored energy (dW/dt).

The plasma community now realizes that merely increasing the auxiliary heating is not sufficient to reach ignition. As external heating is added to the plasma, the turbulence level increases dramatically and more coherent structures appear so that the confinement time is seriously degraded compared to that of lower levels of auxiliary heating.

A less stringent condition derived from the fusion power P_f amplification factor, $Q_f = P_f/P_{\rm loss}$, is maximized at a lower temperature between $10-20\,{\rm KeV}$ where the reaction rate $\langle\sigma v\rangle_{\rm DT} \propto T_i^2$ so that $Q_f \sim n_e\tau_E T \gtrsim 10^{21}\,{\rm m}^{-3}{\rm KeV\,s}$. Here, to reduce the amplification Q_f to the fusion triple product $n_e\tau_E T$, we use $P_f = (1/4)E_f n_e^2\langle\sigma v\rangle_{\rm DT}$, where $E_f = 17.6\,{\rm MeV}$ is the fusion energy release by a D-T reaction and $P_{\rm loss} = nT_E/\tau_E$.

Reference values for the drift wave turbulence parameters in the ITER device are given in Table 1. Coherent structures are now understood to produce intermittent plasma turbulence. There is now a broader level of recognition in the fusion community that an understanding of the chaos and coherent structures created by plasma drift-wave instabilities is required to reach practical fusion energy producing regimes. Let us now examine in detail how the basic

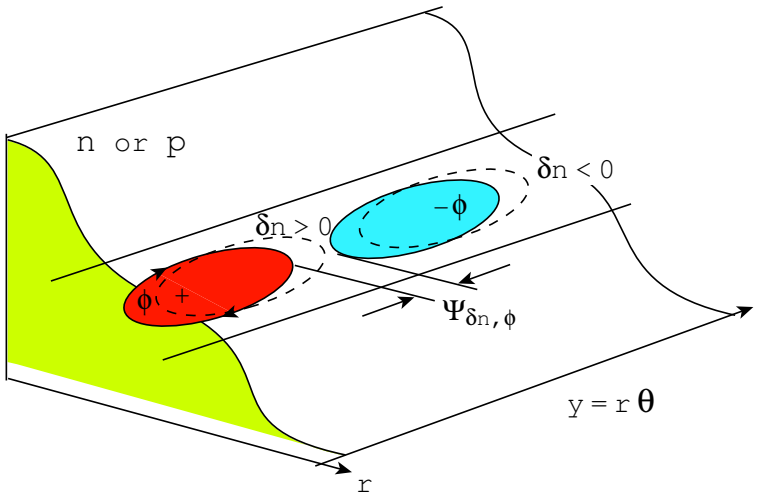

FIGURE 1. The Drift Wave Mechanism

drift-wave mechanism works.

In Fig. 1, we show the profiles of electron density, n_e, and pressure, p_e, along with a drift wave localized over a radial region $\Delta r = \ell_c$, between the two cells in the correlation length. The electrostatic potential that gives rise to the electric field, $\boldsymbol{E} = -\boldsymbol{\nabla}\phi$, is shown by the positive (red) and negative (blue) ovals. Ahead of the potential there are contours of enhanced density ($\delta n_e > 0$) and lower density ($\delta n_e < 0$) phase shifted by $\psi_{\boldsymbol{k}} = \psi(\delta n, \phi)$. The magnetic field is taken to be in the vertical $\boldsymbol{z}$ direction. Thus, the positive potential cell gives a clockwise rotation and the negative cell a counter-clockwise rotation of $\boldsymbol{E} \times \boldsymbol{B}$ convected plasma. Clearly, due the phase shift there is a greater transport of plasma down rather than up the density gradient. Thus, there is a net outward flux of density or pressure given by the y-integrated or time averaged flux $\langle n_e v_r \rangle = \langle n_e E_y / B \rangle$. To be explicit, the model in Fig. 1 and calculation is characterized by the electric potential wave $\phi_k \sin(k_y y - \omega_k t)$ and by the density wave $\delta n_e \sin(k_y y - \omega_k t - \psi_k)$. Calculating the local flux, $\delta n_e v_r$, gives Γ and averaging over y or time gives $\Gamma = \sum_{\boldsymbol{k}} [k_y \phi_k \delta n_k / B] \sin \psi_k$. We will see that the electron response to the potential determines the phase shift ψ_k and amplitude ratio $\delta n_e / \phi_k$. The special case where the phase shift is zero gives $\delta n_e / n_e = e\phi_k / T_e$ and is called the adiabatic response. This adiabatic response is used in many of the classical drift-wave models, e.g. when the temperature gradient drives the drift waves unstable rather than the density gradient ($n \to T$ in Fig. 1). In the turbulent plasma this convective flux occurs at each $\boldsymbol{k}$ with the total being a sum over all scales of k.

We shall see that the typical size of the turbulent cells $\lambda_\perp = 2\pi / k_\perp \sim 6\rho_s$ and the frequency is approximately $\omega_k = k_y v_{de}$, where $v_{de} = -(T_e / eBn_e)(dn_e / dr) = T_e / eBL_n = c_s \rho_s / L_n$. The scale length, $\rho_s = c_s / \omega_{ci}$, is called the ion inertial scale length and determines the scale of the waves and vortex structures. In the quasi-geostrophic flow in planetary atmospheres the equivalent quantity is the Rossby radius [3, p.225]. For reference, a present-day tokamak, e.g. Tore Supra [4] has $R/a = 2.4\,\mathrm{m}/0.72\,\mathrm{m}$, $B = 2\,\mathrm{T}$, $n_e = 3 \times 10^{19}\,\mathrm{m}^{-3}$ and $T_e = 1\,\mathrm{KeV}$. For these parameters $\rho_s / L_n = 0.1\,\mathrm{cm}/80\,\mathrm{cm}$, the sound speed $c_s = 3 \times 10^7\,\mathrm{cm/s}$ and thus $v_{de} = 3 \times 10^4\,\mathrm{cm/s}$ and the drift wave frequency for $k_y = 20\,\mathrm{cm}^{-1}$ is like $6 \times 10^5\,\mathrm{rad/s}$ or 100 kHz. Reference values for ITER included in Table 1. These drift-wave fluctuations have been studied in detail in a wide variety of laboratory machines.

Drift waves are sufficiently slow so that the electrons adjust to the potential fluctuations such that

$$E_\parallel + \frac{1}{en} \boldsymbol{\nabla} p_e = 0. \tag{1}$$

Thus, the waves have the opposite polarization of the MHD waves, which have $E_\parallel = 0$. The parallel electric field, measured in detail in the experiments, is a key part of the drift waves and the related trapped particle mode instabilities. The fluctuating electron current, $\delta j_\parallel$, driven by the parallel electric field takes the energy $\langle \delta j_\parallel E_\parallel \rangle < 0$ out of the nonuniform electron distributions and produces the wave growth. The effect is as though the plasma had a negative resistivity/conductivity $\sigma_\parallel(\omega, \boldsymbol{k})$ for the drift wave.

Detailed measurements and comparisons with theory suggest that, in fact, one of the most serious limiting factor for the success of ITER and similar machines is the control of the drift-wave turbulent transport. The seriousness of the

TABLE 1. ITER [9] and drift wave parameters

Installed auxiliary heating	73 MW
Fusion power	500 MW
Plasma major radius(R)	6.2 m
Plasma minor radius(a)	2.0 m
Plasma volume	830 m^3
Plasma current(I_p)	15 MA
Toroidal field at 6.2 m radius	5.3 T
Density gradient length (L_n)	1 m
Electron temperature (T_e)	10 KeV
Electron Diamagnetic Drift Velocity (v_{de})	1.9 km/s
Ion inertial radius (ρ_s)	0.3 cm
gyro-Bohm diffusivity ($D_{gB} = \rho_s v_{de}$)	5.7 m^2/s
Drift wave frequency ($\omega = k_y v_{de}$)	190 KHz at $k_y\rho_s = 0.3$

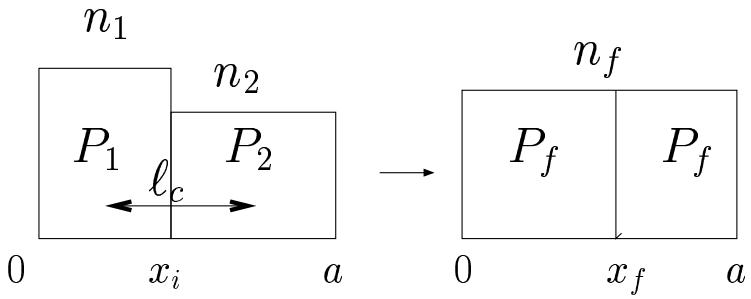

FIGURE 2. Expansion diagram under density gradient $n_1 > n_2$.

turbulence became more evident as machines with increased injected power $P_{\rm aux}$ have reached core power densities of $1\,{\rm MW/m^3}$. The plasma temperature rises only as a fractional power law, like $P_{\rm aux}^{1/2}$, owing to the associated increased turbulence level. The energy confinement time, τ_E, thus decreases even though the temperature increases. The triple product may remain essentially constant.

As a consequence of this stronger heating power, $P_{\rm aux}$, the turbulence is amplified, which shortens the plasma energy confinement time, $\tau_E = W/P_{\rm aux}$, in agreement with the ITER database [5, 6, 7]. The drift-wave turbulence has explained the empirical database laws for both helical systems [8] and Tokamaks [6, 7], showing that $\tau_E = \tau_E^0 (P_0/P_{\rm aux})^{2/3}$. Thus, doubling the $P_{\rm aux}$ shortens the confinement time, $\tau_E \to \tau_E^0/1.59 = 0.64\tau_E^0$. For example, the reference design for ITER (see Table 1) has $P_{\rm ICRF} = P_{\rm ECE} = 20\,{\rm MW}$ and $P_{\rm NBI} = 16\,{\rm MW}$ injected into the plasma volume of $V = 2\pi^2 Rab \simeq 800\,{\rm m^3}$. The average power density is then only $0.07\,{\rm MW/m^3}$. To reach the power density of $1\,{\rm MW/m^3}$ at the core as in current large tokamaks, the ICRH and ECE power need to be focused in the central core volume of $40\,{\rm m^3}$, corresponding to the core radius $r_c = 0.6\,{\rm m}$.

2. ENERGY BOUNDS FOR TURBULENCE

2.1. Density Gradients

The electron drift wave and trapped electron instability (trapped particle mode [10])are driven by the square of the plasma density gradient in plasmas with no background temperature gradient. The wave with a temperature gradient is analyzed in Sec.2.2. In the early literature the electron drift wave with $\gamma_k = (\pi/2)^{1/2}\,\omega_{*e}^2 k_\perp^2 \rho_s^2/|k_\parallel| v_e \propto (dn/dx)^2$ was called the universal instability owing to the drive from $(\nabla n)^2$, which is always present in confined plasmas.

Fig. 2 shows the model for the energy release for the density gradient. The left higher density n_1 (and pressure $p_1 = n_1 T$) box from $x = [0, x_i]$ is allowed to expand to $[0, x_f]$ and compress the gas in the right box until the force

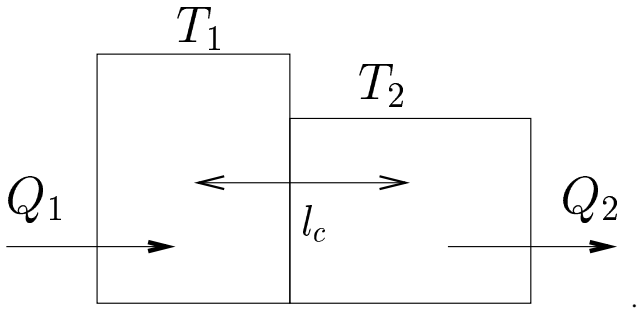

FIGURE 3. Carnot cycle diagram for temperature-gradient driven drift waves

balance is reached with

$$P_f = P_1 \left(\frac{x_i}{x_f}\right)^{\Gamma} = P_2 \left(\frac{a-x_i}{a-x_f}\right)^{\Gamma}. \tag{2}$$

Solving for the new position x_f and calculating the work,

$$W = \frac{1}{a}\int_{x_i}^{x_f} (P_1 - P_2) dx,$$

per unit volume done by the gas during the expansion gives the free energy. For $\Delta x/a \ll 1$, the turbulent energy per unit volume is

$$W_{\rm turb} \le W_{\rm max} = \frac{(\Delta P)^2 x_i (a-x_i)}{\Gamma P a^2} \le \frac{(\Delta P)^2}{4\Gamma P}. \tag{3}$$

If the drift wave energy $W_{\rm turb}$ is almost entirely in the $\boldsymbol{E}\times\boldsymbol{B}$ kinetic energy of the ions, then we have the bound for the average turbulent convection velocity,

$$\left\langle v_E^2 \right\rangle^{1/2} \le \left(\frac{\ell_c}{L_n}\right) c_s \,. \tag{4}$$

When the correlation length ℓ_c is limited by the ion inertial scale length $\ell_c = \rho_s$, the bound for the mean square turbulent plasma velocity is

$$\left\langle v_E^2 \right\rangle \le \left(\frac{\rho_s}{L_n}\right)^2 c_s^2 \equiv v_{de}^2 \,. \tag{5}$$

The limit of $\left\langle v_E^2 \right\rangle \le v_{de}^2$ follows from another argument called the mixing length limit. This argument states that when the gradient of the fluctuating density, $\boldsymbol{\nabla}\delta n$, reaches the value $dn/dx = -n/L_n$ of the ambient density gradient, the gradient source, on average, has been eliminated and growth stops. We then have $\delta n/n = 1/k_x L_n$. With $\ell_c = 1/k_x = \rho_s$, The same amplitude limit applies and the scale of the turbulent diffusion $D_{gB} = \left\langle v_E^2 \right\rangle^{1/2} \ell_c = (\rho_s/L_n)(T_e/eB)$ is defined as the gyro-Bohm diffusivity. To derive the famous Bohm diffusivity, $D_B = T_e/eB$, one instead assumes ℓ_c to be the geometric mean of L_n and ρ_s [11].

2.2. Temperature Gradients

For auxiliarily heated plasmas that develop a temperature gradient $\boldsymbol{\nabla}T$ (either ion or electron) from input power $P_{\rm aux}$, the relevant thermodynamic argument is the Carnot engine.

As shown in Fig. 3, there is an input of energy Q_1 in the left box. The vortices and streamers cycle the plasma over the correlation length ℓ_c, connecting T_1 and T_2. Now, for each cycle, the temperature gradient drives the drift wave to release the energy,

$$W_{\rm turb} \le \Delta W_{\rm carnot} = \Delta S \Delta T, \tag{6}$$

where ΔS is the change in the entropy of the gas. From kinetic theory, the value of the gas constant, Γ, depends on the type of drift wave. $\Gamma = 5/3$ where the wave-particle resonance is $\omega_k = \omega_{\boldsymbol{\nabla}B} + \omega_{\rm curv}$ and $\Gamma = 3$ where $\omega_k = k_\parallel v_\parallel$ and

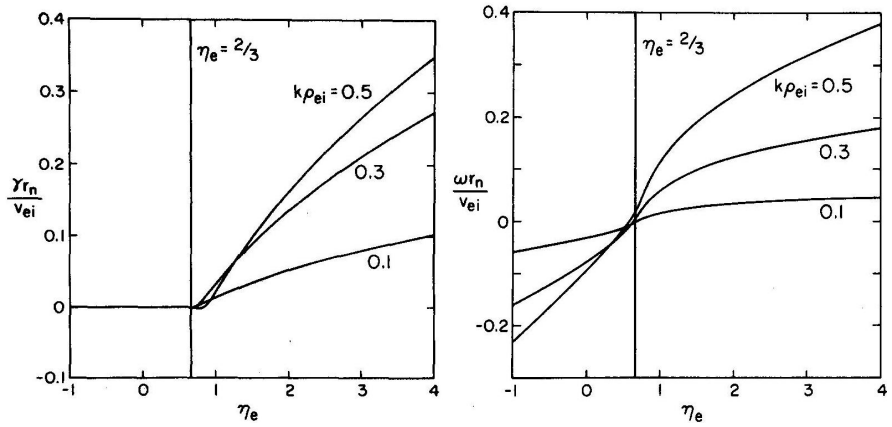

FIGURE 4. The Vlasov (GKE) equation growth rate for the ratio of the temperature gradient length to the density gradient length[12].

$k_\perp \rho_i \ll 1$. For toroidal ITG and ETG, a simple calculation for modes with $\Gamma = 5/3$ yields

$$\Delta S = n\left(\frac{3}{2}\frac{\Delta T}{T} - \frac{\Delta n}{n}\right), \tag{7}$$

which in Eq. (6) together with $\Delta T = -\ell_c dT/dr$ give

$$\Delta W_{\rm carnot} = \frac{3}{2} nT\ell_c^2 \frac{\partial \ln T}{\partial r}\left[\frac{\partial \ln T}{\partial r} - \frac{2}{3}\frac{\partial \ln n}{\partial r}\right]. \tag{8}$$

Fig. 4 shows the roots of the Vlasov-Poisson dispersion relation, $D_{\boldsymbol{k}}(\omega,\mu) = 0$, with increasing $\eta \equiv \boldsymbol{\nabla}\ln T/\boldsymbol{\nabla}\ln n$. Thus, for the kinetic dispersion relation,

$$D_{\boldsymbol{k}}(\omega,\mu) = \frac{1}{T_e} + \frac{1}{T_i}\left[1 - \left\langle \frac{\omega - \omega_{*i}(\eta,\varepsilon)}{\omega - \omega_{Di}\varepsilon + i0^+}\right\rangle\right], \tag{9}$$

where $\varepsilon = E/T_i$ and μ denotes system parameters such as η_i and T_e/T_i. The average $< \cdot >$ is over the local Maxwell phase-space density $f(\varepsilon)$

We find from the Nyquist analysis that the critical temperature gradient is given by

$$\eta_{\rm crit} = \frac{\partial \ln T}{\partial \ln n} = \frac{2}{3}, \tag{10}$$

as shown in Fig. 4. The agreement between the thermodynamical formula and the stability condition of the kinetic dispersion relations can be understood when we see that the wave frequency, $\omega_{\boldsymbol{k}} \simeq 0$ at the critical point. Here the relevant gradient of the phase-space density function $f(r)$ is proportional to $\partial/\partial r[n/T^{d/2}]$ where

$$\frac{\partial f}{\partial r} = \frac{\partial}{\partial r}\left(\frac{n(r)}{T^{d/2}(r)}\right) \quad \text{for} \quad E \ll T, \tag{11}$$

with $\Gamma = (d+2)/d$ for a plasma with d degrees of freedom. For one-dimensional waves like Langmuir waves, $d = 1$ and $\Gamma = 3$, and for toroidal drift waves $d = 3$ and $\Gamma = 5/3$.

The key, universal result given by Eq. (8) for $W_{\rm carnot}$ is that there is only a window of η values, $0 < \eta \leq \Gamma - 1$ which are generally stable. Drift waves are unstable for both inverted gradients $\boldsymbol{\nabla} n \cdot \boldsymbol{\nabla} T < 0$, and strong temperature gradients $\boldsymbol{\nabla} T \gg \boldsymbol{\nabla} n$.

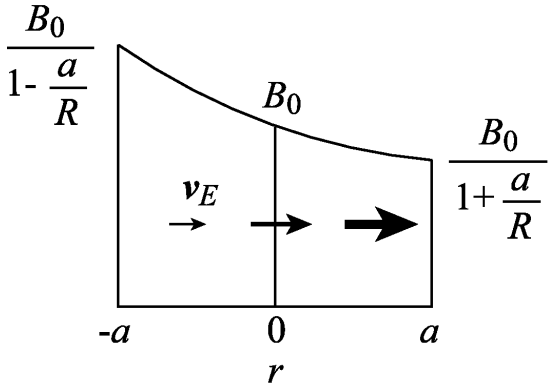

FIGURE 5. Compression/Rarefraction in Convection

3. DRIFT WAVE EIGEN-MODES IN TOROIDAL GEOMETRY

The first effect of toroidal geometry that changes the stability of the drift waves is the unfavorable magnetic field line curvature vector, $\boldsymbol{\kappa} = (\hat{\mathbf{b}}\cdot\boldsymbol{\nabla})\hat{\mathbf{b}} \simeq (\hat{\mathbf{r}}\cos\theta + \hat{\theta}\sin\theta)/R$, which covers the outer half ($\cos\theta > 0$) of the toroidal surfaces. This magnetic curvature creates small scale interchange turbulence with waves that are only partially stabilized by the magnetic shear, $s = rq'/q$, where $q(r) = rB_\phi/RB_\theta$ gives the helical pitch of the field lines. The E_r- shear can also stabilize the modes as discussed in Sec. 4.2. In addition, and closely related, the weakening of the magnetic field with increasing radius (see Fig. 5) leads to an outward acceleration given by the force, $F = -\mu\boldsymbol{\nabla}B$ acting on the plasma.

In the toroidal drift wave equations the local gradients of the density and pressure are normalized with respect to the gradient length, R, of the magnetic field. Thus, the key parameters are

$$\varepsilon_n = \frac{L_n}{R} \quad \text{and} \quad \varepsilon_p = \frac{L_p}{R} \tag{12}$$

throughout the toroidal equations.

The faster radial flows shown in Fig. 5 gives the plasma compression,

$$\boldsymbol{\nabla}\cdot\boldsymbol{v}_E = \frac{2v_x\cos\theta}{R}, \tag{13}$$

compared to the plasma convection,

$$\boldsymbol{v}_E\cdot\boldsymbol{\nabla}n = -\frac{nv_x}{L_n} = -\frac{n}{L_nB}\frac{\partial\Phi}{\partial y}, \tag{14}$$

gives rise to the two terms proportional to $(1-2\varepsilon_n\cos\theta)\omega_{*e}$ in the drift-wave eigen-mode equation.

The density and potential fluctuations set up along the magnetic field line give rise to ion acoustic waves with $\omega^2 = k_\parallel^2 c_s^2$, where

$$k_\parallel^2 \to -\frac{1}{q^2R^2}\left(\frac{\partial}{\partial\theta} + q(r)\frac{\partial}{\partial\phi}\right)^2 \tag{15}$$

is a differential operator.

Similarly, the shear-Alfvén wave $\omega^2 = k_\parallel^2 v_A^2$ propagates with the $k_\parallel^2$ operator. The periodicity of the torus means that a physical field is the same at $(\theta + 2\pi m, \phi + 2\pi n)$ for all integer values of m,n. These rational surfaces appear when the pitch of the magnetic field is the same as that of the mode $\exp(im\theta - in\phi)$, which occurs when the RHS of Eq. (15) vanishes. The compressional term in Eq. (13) and convection term in Eq. (14) combine with the ion acoustic waves to make the drift wave eigen-mode equation for waves of the form,

$$\Psi(x,t) = \sum_m \Phi_{m,n}(r)e^{im\theta - in\phi - i\omega t} + c.c. = \Phi(r,\theta)e^{-in\phi - i\omega t} + c.c. \tag{16}$$

The toroidal mode solution, $\Phi(r,\theta)$ of this Mathieu-type equation is for each given r determined by

$$\frac{c_s^2}{\omega^2 q^2 R^2}\left(\frac{\partial}{\partial\theta}-inq(r)\right)^2\Phi+\left[1-i\delta_{\boldsymbol{k}}-\rho_s^2\nabla_\perp^2-\frac{\omega_{*e}}{\omega}(1-2\varepsilon_n\cos\theta)\right]\Phi=0. \tag{17}$$

Here we used the simple phase-shifted, non-adiabatic electron response, $\delta n_e = n_e(e\phi/T_e)(1-i\delta_{\boldsymbol{k}})$. Introducing the phase variation $\Phi\rightarrow\Phi(\theta)e^{inq(r)\theta}$, required to keep $k_\parallel^2\Phi$ small, we find that $\nabla_\perp^2\Phi=(\partial_r^2+r^{-2}\partial_\theta^2)\Phi e^{inq\theta}=-(k_r^2+k_\theta^2)=-k_\theta^2(1+s^2\theta^2)\Phi$, where $k_r=sk_\theta\theta$ and $k_\theta=nq/r$.

The drift-eigen-mode equation for the one-dimensional ansatz $\Phi(\theta)$ is called the "ballooning mode" equation, which from Eqs.(15 - 17) is

$$\frac{c_s^2}{\omega^2 q^2 R^2}\frac{\partial^2\Phi}{\partial\theta^2}+\left[1-i\delta_{\boldsymbol{k}}+k_\theta^2\rho_s^2(1+s^2\theta^2)-\frac{\omega_{*e}}{\omega}(1-2\varepsilon_n\cos\theta)\right]\Phi=0\,. \tag{18}$$

The solution of Eq. (18) with a shooting code requires as a boundary condition such that when $\theta^2\rightarrow\infty$ the solution $\Phi\rightarrow\exp(i\frac{\sigma}{2}\theta^2)$, where $\sigma=\omega qR|sk_\theta|\rho_s/c_s$ with $\mathrm{Im}\,\sigma\propto\mathrm{Im}\,\omega>0$. When the mode is strongly localized to the small θ^2 region, we may use $\cos\theta\simeq 1-\theta^2/2$ to reduce Eq. (18) to the analytic harmonic oscillator problem with eigenvalues,

$$\omega_{k_\theta,n}=\frac{\omega_{*e}(1-2\varepsilon_n)-ic_s|sk_\theta|\rho_s/(qR)(2n+1)}{1+k_\theta^2\rho_s^2-i\delta_{\boldsymbol{k}}} \tag{19}$$

and eigen-functions, $\Phi_n(\theta)=\exp(i\frac{\sigma}{2}\theta^2)H_n((-i\sigma)^{1/2}\theta)$. Thus, the magnetic shear, $|s|$, introduces a damping of the waves due to the coupling to the ion acoustic waves that the propagate wave energy to region of Landau damping. Marginal stability conditions follow from Eq. (19) once the details of the dissipative $\delta_{\boldsymbol{k}}(\mu)$ function are given.

4. LABORATORY DRIFT WAVE EXPERIMENTS

4.1. Identification of Drift Waves

Let us now examine how these drift waves arise in simple geometries and what has been measured with probes in university-scale drift wave experiments.

The first detailed study of the drift wave growth, saturation and anomalous transport was in a series of Q-machine experiments [13]. Hendel et al. [13] and Chen [14] describe the identification of the mode frequencies and wavelengths in detail with variation of the system parameters in the Q-machine. The linear growth rate, $\gamma_{\boldsymbol{k}}=\mathrm{Im}\,\omega$, is produced by the phase shift, $\psi_{\delta n,\phi}$, from the electron collisions, ν_e, resulting in a density response,

$$\frac{\delta n_e}{n_e}=\frac{\omega-\omega_{*e}+ik_\parallel^2v_e^2/\nu_e}{\omega+ik_\parallel^2v_e^2/\nu_e}\frac{e\phi_{\boldsymbol{k}}}{T_e}, \tag{20}$$

from the potential wave $\phi_{\boldsymbol{k}}$. The growth rate, $\gamma_{\boldsymbol{k}}$, was controlled in the experiments by varying the ion viscosity μ, where $\mu/\rho_m=(3/10)\nu_i\rho_i^2$, ν_i is the ion collision frequency, ρ_i the ion gyroradius and ρ_m the mass density. Since $\mu/\rho_m\propto 1/B^2$, the experimentalists varied the B-field through the critical value, $\boldsymbol{B}_{\rm crit}$, to measure the growth rate directly as well as the wave frequency. The nonlinear saturation occurs when the nonlinearity in the ion dynamics balances the growth rate from the electrons. This type of nonlinear saturation is generic to drift waves since the rapid electron motion leaves the electron phase as in the linear response theory. In section 6 we show these nonlinear features in more detail.

The first clear measurements of the ITG drift mode in a tokamak was provided by Brower et al. [15] (see Fig. 6) using laser scattering in the TEXT tokamak. This TEXT data used a Heavy Ion Beam Probe (HIBP) to measure both the DC radial electric field, E_r, and the local fluctuating potential, $\delta\phi(\boldsymbol{x},t)$. The plasma density fluctuation, δn_e, was measured with a 6-channel CO_2 laser-scattering diagnostic that yields $\boldsymbol{k}=\boldsymbol{k}_{\rm out}-\boldsymbol{k}_{\rm in}$ from the Bragg scattering condition of the outgoing $\boldsymbol{E}_{\boldsymbol{k}_{\rm out}}$ and incoming $\boldsymbol{E}_{\boldsymbol{k}_{\rm in}}$ electromagnetic waves from the plasma wave $\delta n_e(\boldsymbol{k})$. The wave number, k_θ, is shown on the axis in Fig. 7. The frequency in the laboratory frame is shown on the $\boldsymbol{y}$-axis, which includes the Doppler shift $\boldsymbol{k}\cdot\boldsymbol{v}_E=-(E_r/B)k_\theta$, where $\boldsymbol{v}_E$ is derived from HIBP data that measures E_r.

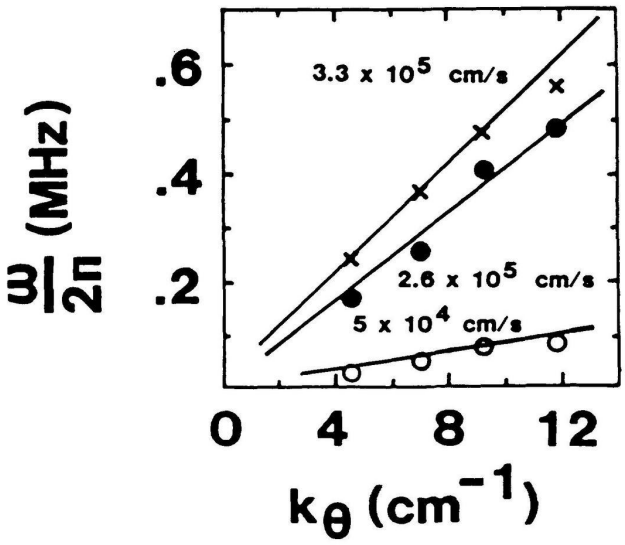

FIGURE 6. Microturbulence statistical dispersion for electron components, $n_e = 2 \times 10^{13}\,\mathrm{cm}^{-3}$(crossed), $2 \times 10^{13}\,\mathrm{cm}^{-3}$(filled circles) and ion component $n_i = 8 \times 10^{13}\,\mathrm{cm}^{-3}$(open circles)[15]

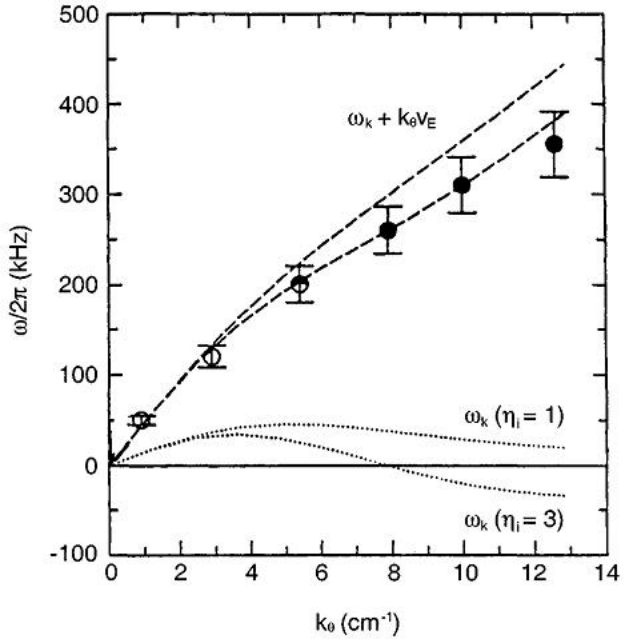

FIGURE 7. The frequency of the electron density fluctuation in the laboratory versus the azimuthal wave number k_θ for scattering.

For the TFTR machine Fig. 8 gives the estimate of the density fluctuation level $\delta n/n$ as a function of increasing neutral beam (NB) heating power P_{NB}. At the left, the data for $P_{\mathrm{NB}} = 0$ is for the ohmic discharge with very low $\delta n/n \simeq 0.001$. As the beam heating power increases, the fractional fluctuations rise to 0.003 at 5 MW, 0.006 at 9 W and 0.015 at 19 MW. This increase of $\delta n/n$ is consistent with power balance $< nT > /\tau_E = (P_{\mathrm{NB}} + P_{\mathrm{Oh}})/\mathrm{Vol}$ with

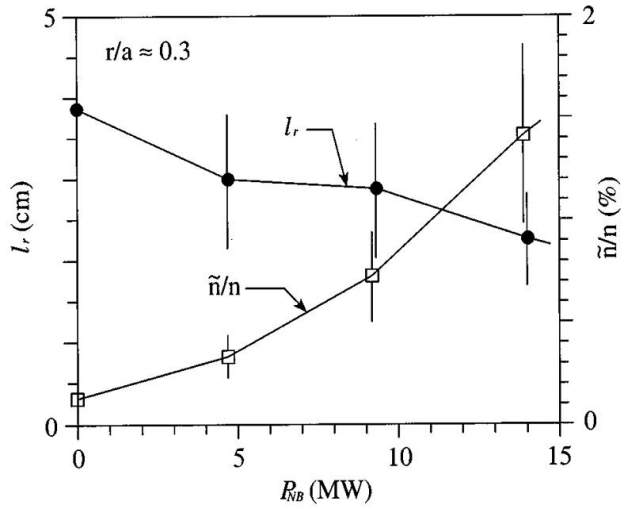

FIGURE 8. Power scan in TFTR microwave scattering for the density radial scale length (circles) and density fluctuation level (squares) as a function of NB power at $r/a \simeq 0.3$[16].

$1/\tau_E \propto \chi_{gB}/a^2 \propto T^{3/2}$. Here Vol is the mean plasma volume determined by the mean value theorem,

$$\int \frac{3}{2} nT \mathrm{d}^3 r = \frac{3}{2} < nT > \cdot Vol. \tag{21}$$

In tokamaks with higher temperatures and thus stronger radial temperature gradients, the drift wave changes character and is destabilized by the ion temperature gradient, $\boldsymbol{\nabla} T_i$. In this regime, called the ion temperature gradient (ITG) instability, the electron dissipation $i\delta_{\boldsymbol{k}}$ can be dropped and the electron response taken as adiabatic and is therefore defined by $\delta n_e/n_e = e\phi_{\boldsymbol{k}}/T_e$.

Simpler basic experiments validating the ITG model were carried out in the Columbia Linear Machine (CLM) as given in Sen et al. [17]. These plasmas, produced by RF heating, have $n_e \sim 2 \times 10^{14}\,\mathrm{m}^{-3}$ and $T_i \sim 10\,\mathrm{eV}$. There is a temperature anisotropy $T_{i\|} \neq T_{i\perp}$ that complicates the linear dispersion but is useful for both NBI or RF heated toroidal experiments and the central cell of the tandem mirror. In the GAMMA-10 tandem mirror resonant ion cyclotron heating in the central cell results in $T_{i\perp} \sim 6.5\,\mathrm{KeV}$ and $T_{i\|} \sim 2.5\,\mathrm{KeV}$[18]. The details of the two temperature components of the ITG theory with the simple cylindrical central-cell plasma data can be found in Hojo [19] and Sen et al. [17].

In section 6, we will discuss the free energy of the ITG modes and their simulation in the gyro-kinetic Vlasov system. The literature concerning the numerical modeling of ITG modes is extensive due to its role as the standard model for explaining the anomalous ion thermal diffusivity, χ_i.

4.2. The effect of magnetic and E_r shear on drift waves

The amplitude of the ITG turbulence is controlled by the magnetic shear, $s = rq'/q$, and the shear in the azimuthal (or poloidal) flow velocity, $v_E = -E_r/B$. For example, Hamaguchi and Horton [20, 21, 22] show, with an FLR fluid model, the variation of the amplitudes and the resulting turbulent ion heat flux, $q_i = \langle n_i T_i v_r \rangle$, with magnetic and E_r shears. Kishimoto et al. [23] showed similar results with a PIC code. In the toroidal code, the shear, v'_E, from E_r stifles the χ_i transport, whereas suppression of χ_i in the local slab model is given by

$$\chi_i(v'_E) = \frac{\chi_i}{1 + (L_s v'_E/c_s)^2}, \tag{22}$$

as shown in Terry [24] and Newman et al. [25]. Here $L_s = qR/s(r)$ is the shear length defined by the distance spanned by the magnetic field when the $\boldsymbol{B}$-vector rotates by approximately $\pi/4$. The physical picture of the velocity-shear effect is given in Biglari et al. [26] where the large eddies or vortices of size $\Delta r = \rho_s(L_s/L_T)$ in the absence of shear flows are reduced in the shearing time, $\tau_{\mathrm{sh}} = 1/v'_E$, to small eddies. The details of the shear flow stabilization are complicated,

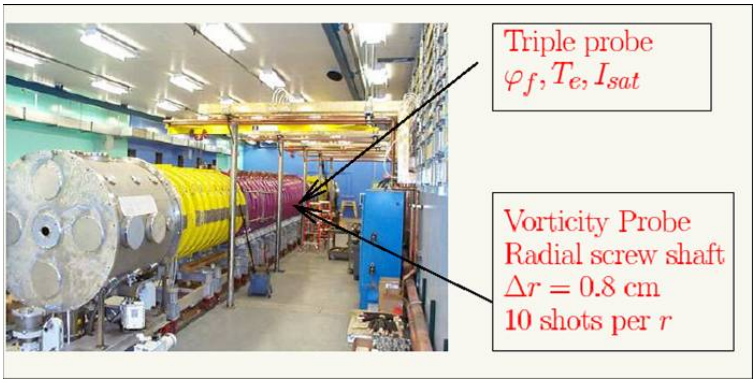

FIGURE 9. LAPD machine ($L = 17\,\mathrm{m}$, $a = 0.5\,\mathrm{m}$) with the location of the triple probe and the vorticity probe driven on a a shift taking 10 shots per $\Delta r = 0.8\,\mathrm{cm}$ through the region of drift wave and Kevin Helmholtz turbulence.

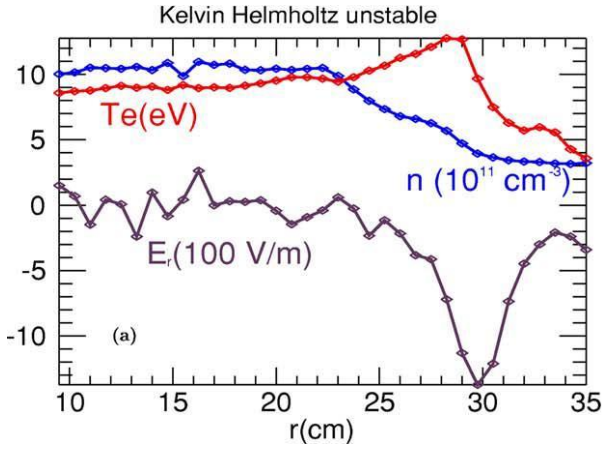

FIGURE 10. Mean profiles obtained as an average in 25 experimental shots during the stationary turbulent state during the wall-bias pulse [30]

see P.H. Diamond's chapter of the proceedings. A kinetic theory calculation is given by Dong et al. [27] and the role of shear flow in magnetized plasma is reviewed by Itoh and Itoh [28], Terry [24], Diamond et al. [29].

Experiments for validation of drift-wave theory were performed on LAPD (Fig. 9). These regimes were created by varying the radial electric field, E_r, from weak to moderate and then to strong. In the moderate and strong E_r regime, the electron-density transport barrier was measured as shown in Fig. 10. The main characteristic of the drift wave was identified clearly in the weak E_r-shear regime and the mixed Kelvin-Helmholtz drift-wave regime.

In the strong E_r-shear regime there is a deep well of negative E_r – as occurs in the edge of H-mode tokamak plasmas. The vorticity probe measures $\omega_z = \hat{\mathbf{b}} \cdot \nabla \times \boldsymbol{v}_E$ (see Fig. 11).

As the probe sweeps across the shear layer, the vorticity changes from counter-clockwise to clockwise rotating vortices, just as expected from simple considerations and computer simulations. The region between these two oppositely spinning vortices forms the partial transport barrier as suggested by Biglari et al. [26] and Terry [24].

The strong shear flow in a plasma creates temporal and spatial intermittency as shown by the probability distribution function with large skewness and excess probability levels over the gaussian level (red parabola) in Fig. 11. In the central cell of the GAMMA-10 tandem mirror, where the electron temperature $T_e \sim 800\,\mathrm{eV}$, there is sufficient soft-X-ray emission to image the growth and decay of the vortices using two micro-channel plates and tomographic image reconstruction [31, 18]. In Fig. 12, the X-ray tomography shows such an event over the rotational period of $50\,\mu\mathrm{s}$. The growth and decay of vortex structures are clearly seen. Moreover, they appear consistent with simulations by Kim et al. [32], which show vortex intermittency in sheared flows.

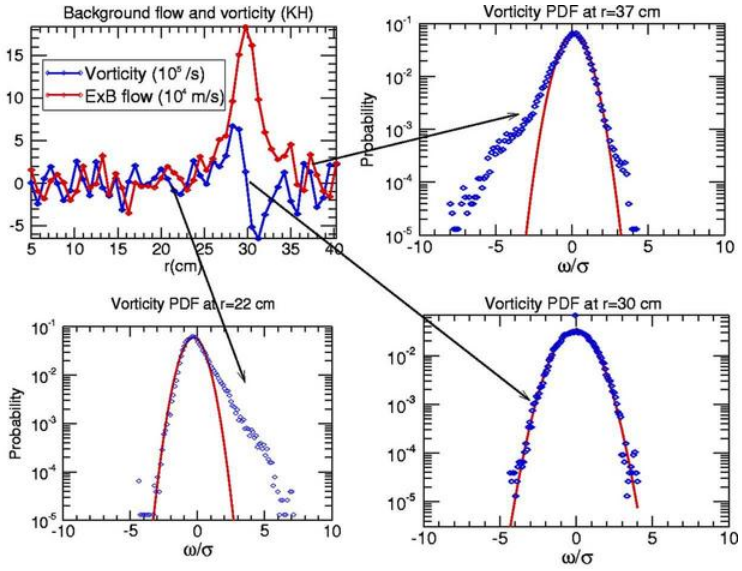

FIGURE 11. Vorticity probabiliy distribution functions for representative radius in strong the E_r-shear regime[30].

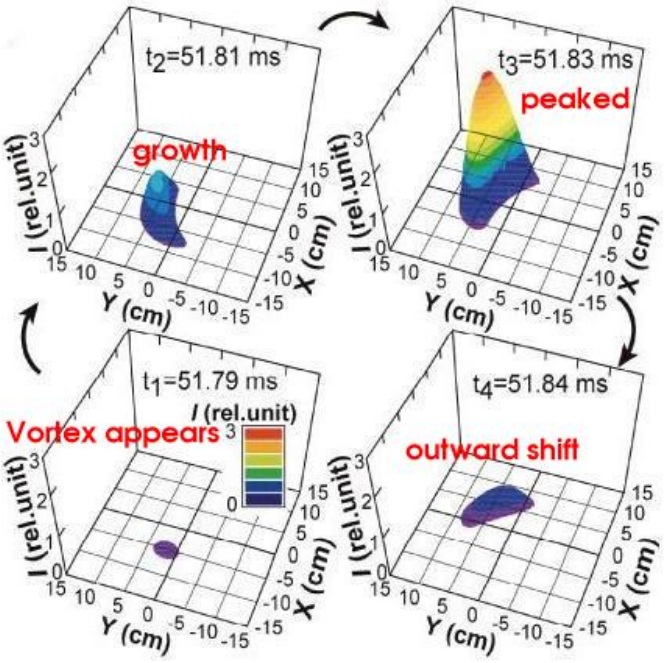

FIGURE 12. X-ray tomography of a detailed vortex structure of an intermittent object showing its typical lifetime ranging around a hundred microseconds, approximately with the rotational motion of an $\boldsymbol{E} \times \boldsymbol{B}$ drift[31].

4.3. Electromagnetic scattering from turbulent density fluctuations

Non-perturbative measurements of the plasma fluctuation are carried out with Bragg scattering, $\boldsymbol{k} = \boldsymbol{k}_{\rm out} - \boldsymbol{k}_{\rm in}$, where an in coming micro-wave or lower wave, $\boldsymbol{E}_{\rm in}\exp(i\boldsymbol{k}_{\rm in}\cdot\boldsymbol{x} - i\omega_{\rm in}t)$, sets the electron into quiver motion with $\delta\boldsymbol{v}_e = -e\boldsymbol{E}_{\rm in}/im_e\omega_{\rm in}$ that radiates $\boldsymbol{E}_{\rm out}\exp(i\boldsymbol{k}_{\rm out}\cdot\boldsymbol{x} - i\omega_{\rm out}t)$, with current $\delta\boldsymbol{j} = -e\delta n_{\boldsymbol{k}}\delta\boldsymbol{v}_{\boldsymbol{e}}(\boldsymbol{k}_{\rm in})$. The scattered wave, $\boldsymbol{E}_{\rm out}\exp(i\boldsymbol{k}_{\rm out}\cdot\boldsymbol{x} - i\omega_0 t)$ has $\boldsymbol{k}_{\rm out} = \boldsymbol{k} + \boldsymbol{k}_{\rm in}$ and $\omega_{\rm out} = \omega_{\boldsymbol{k}} + \omega_{\rm in}$. Since $\omega_{\boldsymbol{k}} \ll k_{\rm in}c$, the frequency shift is often

too small to be useful. The scattering cross-section, $d\sigma/d\Omega = (e^2/m_e c^2)^2 \left\langle |\delta n_e(\boldsymbol{k})|^2 \right\rangle \Omega_{scat}/n_e$, where Ω_{scat} is the scattering volume defined by the insertion of the two electromagnetic waves giving a non-perturbative measurement of $\langle |\delta n_e(\boldsymbol{k})|^2 \rangle$. Both X- and O-mode polarizations are useful [33].

In 1976 electromagnetic scattering experiments, by Mazzucato [16] on the ATC machine and by Slusher and Surko [34] on Alcator, showed clearly the presence of substantial drift wave turbulence. The weak turbulence mode coupling theory was used in Horton [35] to give, within error bars, the level of $|\delta n(\boldsymbol{k}_\perp)|$ at the six $k_\perp$ ranging from $1/2.3$ to $1/0.4\,\mathrm{cm}^{-1}$ used in ATC. This type of scattering data is shown in Fig. 8 for TFTR. Use of scattering from O- to X-mode polarization gives a measure of $\left\langle |\delta B_r(\boldsymbol{k})|^2 \right\rangle$ in Zou et al. [36] and in Colas et al. [37] in the core of Tore Supra.

The cross-polarization experiments by Colas et al. [37] show $\delta B_x^2/B^2$ increasing up to levels of $\delta B_x/B_0 \simeq 5\times 10^{-5}$ with higher heating power and $\boldsymbol{\nabla} T_e$. The interpretation of the cross-polarizing experiments is difficult since part of the O→X-mode conversion can also be scattered power that can arise from internal reflection in the machine. These experiments and their interpretation are discussed further in the chapter by P. Hennequin.

5. WEAK TURBULENCE THEORY FOR DRIFT WAVES

For turbulent states with a broad range of wavenumbers, $\Delta\boldsymbol{k}$, and frequencies, $\Delta\omega_{\boldsymbol{k}}$, in the fluctuation spectrum the Weak Turbulence Theory is developed by assuming that the deviation of the fluctuations from Gaussian statistics is weak. Under this condition the chain of coupled correlation functions is broken off at fourth order with what is called the "quasi-normal closure approximation". This means that the ensemble average of the product of four $\phi_{\boldsymbol{k}}$ fields is factorized as

$$\left\langle \phi_{\boldsymbol{k}_1}\phi_{\boldsymbol{k}_2}\phi_{\boldsymbol{k}_3}\phi_{\boldsymbol{k}_4=-\boldsymbol{k}_1-\boldsymbol{k}_2-\boldsymbol{k}_3}\right\rangle = \left\langle \phi_{\boldsymbol{k}_1}\phi_{\boldsymbol{k}_2}\right\rangle\left\langle \phi_{\boldsymbol{k}_3}\phi_{\boldsymbol{k}_4}\right\rangle + \left\langle \phi_{\boldsymbol{k}_1}\phi_{\boldsymbol{k}_3}\right\rangle\left\langle \phi_{\boldsymbol{k}_2}\phi_{\boldsymbol{k}_4}\right\rangle + \left\langle \phi_{\boldsymbol{k}_1}\phi_{\boldsymbol{k}_4}\right\rangle\left\langle \phi_{\boldsymbol{k}_2}\phi_{\boldsymbol{k}_3}\right\rangle, \tag{23}$$

which closes the equations for the dynamics of $I_{\boldsymbol{k}}(t) = \left\langle \phi^*_{\boldsymbol{k}}\phi_{\boldsymbol{k}}\right\rangle$.

For drift waves the energy spectrum,

$$W_{\boldsymbol{k}} = (1+k_\perp^2\rho_s^2) I_{\boldsymbol{k}}(t), \tag{24}$$

and the resulting weak-turbulence wave-kinetic equation is

$$\begin{aligned}\frac{dW_{\boldsymbol{k}}}{dt} &= 2\gamma_{\boldsymbol{k}} W_{\boldsymbol{k}} + \sum_{\boldsymbol{k}_1,\boldsymbol{k}_2=\boldsymbol{k}-\boldsymbol{k}_1} \frac{(\boldsymbol{k}\times\boldsymbol{k}_1\cdot\hat{\boldsymbol{z}})^2}{B^2}(k_2^2-k_1^2) R_{\boldsymbol{k},\boldsymbol{k}_1,\boldsymbol{k}_2}\cdot \\ &\qquad \left[(k_2^2-k_1^2)W_{\boldsymbol{k}_1}W_{\boldsymbol{k}_2} - (k^2-k_1^2)W_{\boldsymbol{k}}W_{\boldsymbol{k}_1} + (k^2-k_2^2)W_{\boldsymbol{k}}W_{\boldsymbol{k}_2}\right],\end{aligned} \tag{25}$$

with the resonance function given by

$$R_{\boldsymbol{k},\boldsymbol{k}_1,\boldsymbol{k}_2} = -\mathrm{Im}\left[\frac{1}{\omega_{\boldsymbol{k}} - \omega_{\boldsymbol{k}_1} - \omega_{\boldsymbol{k}_2} + i(\nu_{\boldsymbol{k}} + \nu_{\boldsymbol{k}_1} + \nu_{\boldsymbol{k}_2})}\right] \simeq \pi\delta(\omega_{\boldsymbol{k}} - \omega_{\boldsymbol{k}_1} - \omega_{\boldsymbol{k}_2}), \tag{26}$$

for $\nu_{\boldsymbol{k}} \ll \max(\omega_{\boldsymbol{k}})$. In the classical model with adiabatic electrons, the wave-kinetic equation obeys the conservation laws of energy, $d/dt\sum_{\boldsymbol{k}} W_{\boldsymbol{k}} = 0$, and enstropy, $d/dt\sum_{\boldsymbol{k}}(1+k_\perp^2)W_{\boldsymbol{k}} = 0$.

These two invariants lead to the cascade of enstropy, $\Omega = \sum_{\boldsymbol{k}} k_\perp^2 W_{\boldsymbol{k}}(t)$, to high $\boldsymbol{k}_\perp$ and the inverse cascade of energy W to low $\boldsymbol{k}_\perp$. The equilibrium solution of the wave-kinetic equation with no growth/damping, i.e. $\gamma_{\boldsymbol{k}} \equiv 0$, is the equipartition of the energy $W_{\boldsymbol{k}} = W_{\mathrm{total}}/N_{\mathrm{modes}}$, where N_{modes} is the total number of modes.

In reality, there are limited regions of $\boldsymbol{k}$-space where $\gamma_{\boldsymbol{k}} > 0$ and hence where modes can grow from the gradient mechanism in Sec. 1. In all other regions modes are damped. While some approximate analytic solutions to Eqs. (24-26) are known in terms of anisotropic Kolmogorov-type spectra $1/|k_x|^{m_x}|k_y|^{m_y}$, the general solution to the problem can only be found numerically.

Fig. 13 shows by the shaded loop in $\boldsymbol{k}$-space the region of resonant three-wave interaction defined by the subspace $\omega(\boldsymbol{k}) - \omega(\boldsymbol{k}_1) - \omega(\boldsymbol{k}_2) = 0$. There are two special parts of this resonant manifold : one where $\boldsymbol{k}_1 = (2k_x, 0)$, which is a zonal flow type of state with $u_y(x) = k_x\phi_{\boldsymbol{k}_1}\sin(2k_x x)$ and $u_x = 0$, and the the second is the quasi-adiabatic part of the resonant manifold where two neighboring waves $(\boldsymbol{k}_1, \boldsymbol{k}_2)$ resonate, i.e. $(\boldsymbol{k},\omega_{\boldsymbol{k}}) - (\boldsymbol{k}_2,\omega_{\boldsymbol{k}_2}) = (\boldsymbol{k}_1,\omega_{\boldsymbol{k}_1})$ with small values of $\boldsymbol{k}_1$ and $\omega_{\boldsymbol{k}_1}$. This second class gives a scale separation where the symbols $\boldsymbol{q} = \boldsymbol{k}_1 \ll |\boldsymbol{k}|$ and $\Omega = \omega_{\boldsymbol{k}_1} \ll |\omega_{\boldsymbol{k}}|$

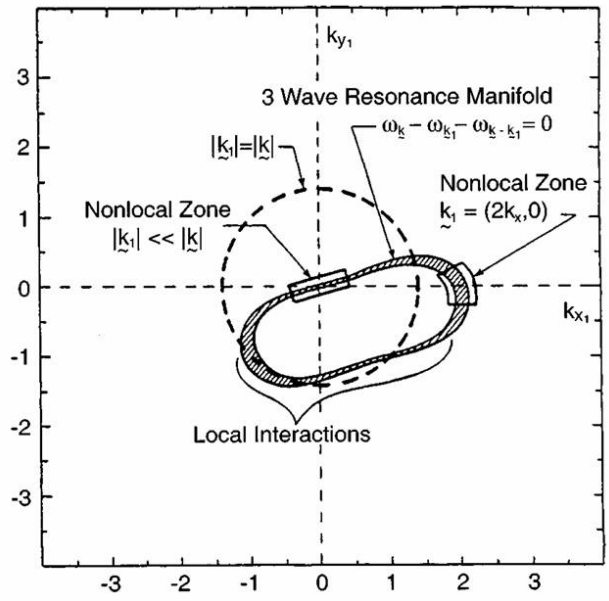

FIGURE 13. Wave-resonance manifold

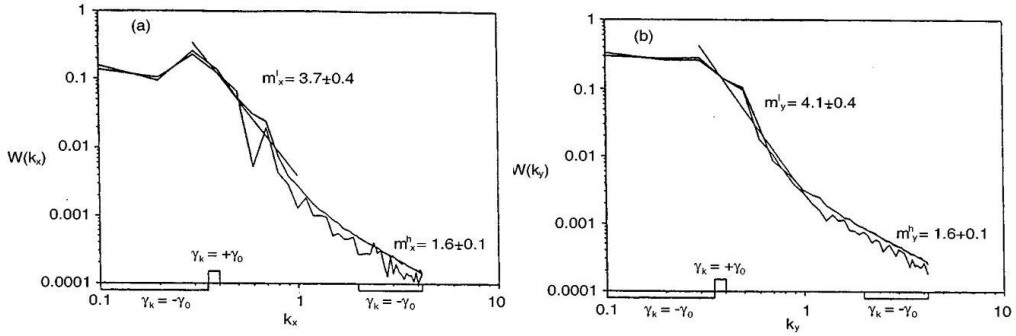

FIGURE 14. Drift-wave spectrum for model with isotropic ring of unstable modes, $\gamma_0 > 0$, for $0.35 < k < 0.4$ and high k damping for $k > 2$.

are often introduced for the large scale part of the spectrum. These cross-scale $\boldsymbol{k} \leftrightarrow \boldsymbol{q}$ interactions give a long-range energy transfer in $\boldsymbol{k}$-space. These two regions of special interest are marked by rectangles in Fig. 13.

Fig. 14 shows an example of the anisotropic Kolmogorov spectrum applied, where there is only an unstable ring for $0.35 < (k_x^2 + k_y^2)^{1/2} \leq 0.4$ with small $\gamma_0 > 0$ and damping of $-\gamma_0$ at both high $\boldsymbol{k}$ and low $\boldsymbol{k}$. The steady state spectra of $W(k_x) = \sum_{k_y} W(k_x, k_y) \simeq 1/|k_x|^{m_x}$ and $W(k_y) = \sum_{k_x} W(k_x, k_y) = 1/|k_y|^{m_y}$ are shown in Fig. 14. We see that most of the turbulent energy has accumulated in $\boldsymbol{k}$'s below the growth region $(k_\perp \sim 0.35)$, while the region above the growth region has a power-law decay with $m_x = 3.7 \pm 0.4$ and $m_y = 4.1 \pm 0.4$. These results are typical but not universal for drift wave turbulence.

The adiabatic electron model leads to that the nonlinear $\boldsymbol{E} \times \boldsymbol{B}$ convection of the density by $\boldsymbol{v}_E \cdot \boldsymbol{\nabla} n = 0$ vanishes. In general however, there is an appreciable non-adiabatic part of the density response to ϕ as in Eq. (20). The non-adiabatic part, for example, $\delta n = (1 + \delta_0 \partial/\partial y)\phi \rightarrow (1 + i\delta_0 k_y)\phi_{\boldsymbol{k}}$ leads to a nonlinear $\boldsymbol{E} \times \boldsymbol{B}$ drift $\boldsymbol{v}_E \cdot \boldsymbol{\nabla} n \neq 0$ and turbulent transport for $\delta_0 \neq 0$. Waltz has shown that the additional nonlinear term from $\boldsymbol{v}_E \cdot \boldsymbol{\nabla} n$ leads to a lower amplitude as shown in Fig. 15. The values of $\phi_{\rm rms} = \left\langle \phi^2 \right\rangle^{1/2}$ and the diffusivity D are shown as a function of the non-adiabatic parameter δ_0.

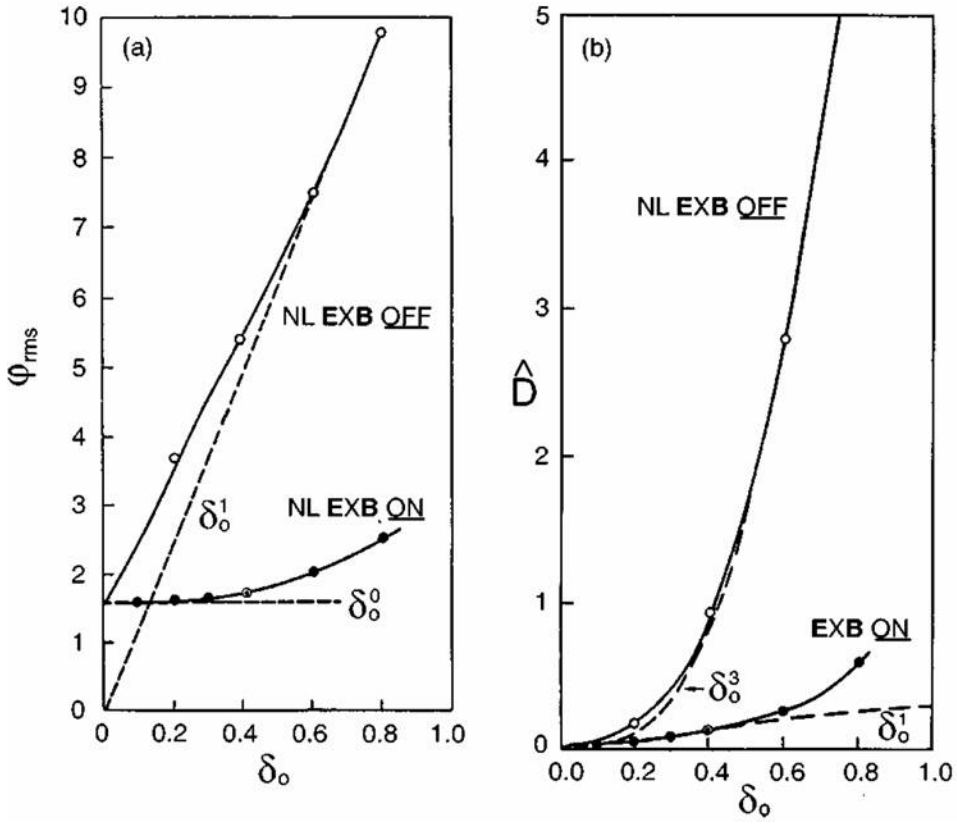

FIGURE 15. Waltz simulation comparing the saturation levels of the Hasegawa-Mima model with NL (nonlinear $\boldsymbol{v}_E \cdot \boldsymbol{\nabla}\delta n$) off and the Terry-Horton model with $\boldsymbol{v}_E \cdot \boldsymbol{\nabla}\delta n$ turned on.

6. ION TEMPERATURE GRADIENT MODE

There are numerous nonlinear formulations of the ion temperature gradient mode in the literature. The models range from one-field models (e.g. Hasegawa-Mima) with one nonlinearity $\boldsymbol{v}_E \cdot \boldsymbol{\nabla}$, to two field-models; both of them include the fluctuating electrostatic potential ϕ. The one-field model, however, uses the the adiabatic electron response $\delta n_e/n_e = e\phi/T_e$ for the density fluctuation whereas the two-field model uses either the fluctuating ion pressure, δp_i, or the fluctuating ion temperature, δT_i, dynamical equation. These gyro-fluid models assume a closure that can be either an equation of state with adiabatic gas constant, Γ, for the ion fluid or closure formulas for the parallel ion-thermal-heat flux, $\delta q_{i\|}$ [38, 39, 40]

References describing different models are Horton et al. [41], Hamaguchi and Horton [20], Dimits et al. [42] for the slab ITG mode and Horton et al. [43], Waltz et al. [44], Beer and Hammett [45] for the toroidal ITG mode. The toroidal ITG mode is typically stronger than the slab ITG mode and has a mathematical structure similar to a small scale ($\lambda_\perp \gtrsim \rho_i$) Rayleigh-Taylor instability. The Rayleigh-Taylor MHD instability,

$$\omega^2 = -\gamma_{\rm MHD}^2 = \frac{k_y^2}{k_\perp^2}\left(\frac{1}{\rho_s}\frac{dp}{dx}\frac{1}{R_c}\right) \gg k_\|^2 v_A^2, \tag{27}$$

is changed in drift-wave theory to a slower growing mode with $\gamma(k_y = 0) = 0$ and a well-defined maximum growth rate, $\gamma_{\max}$, at a finite $k_y\rho_s \simeq [(1-2\varepsilon_n)/(1+\eta_i)]^{1/2}$. Here $\varepsilon_n = L_n/R$ and $\eta_i = {\rm d}\ln T_i/{\rm d}\ln n_i$. The electrostatic shielding by the adiabatic electron fluid that has a dielectric constant, $\varepsilon = 1 + 1/k_\|^2\lambda_{De}^2 \gg 1$, since $k_\|\lambda_{De} = k_\| v_e/\omega_{pe} \ll 1$. The energy source of the instability is explained in Sec. 2.2. The typical $\gamma_{\max} = 0.1c_s/(L_{Ti}R)^{1/2}$ for a toroidal system with a magnetic radius of curvature, $R_c = R$, on the outside of the torus where the mode balloons. The ballooning-mode equation and a simple nonlinear model for the toroidal ITG are given in Horton et al. [43]. Here we give the

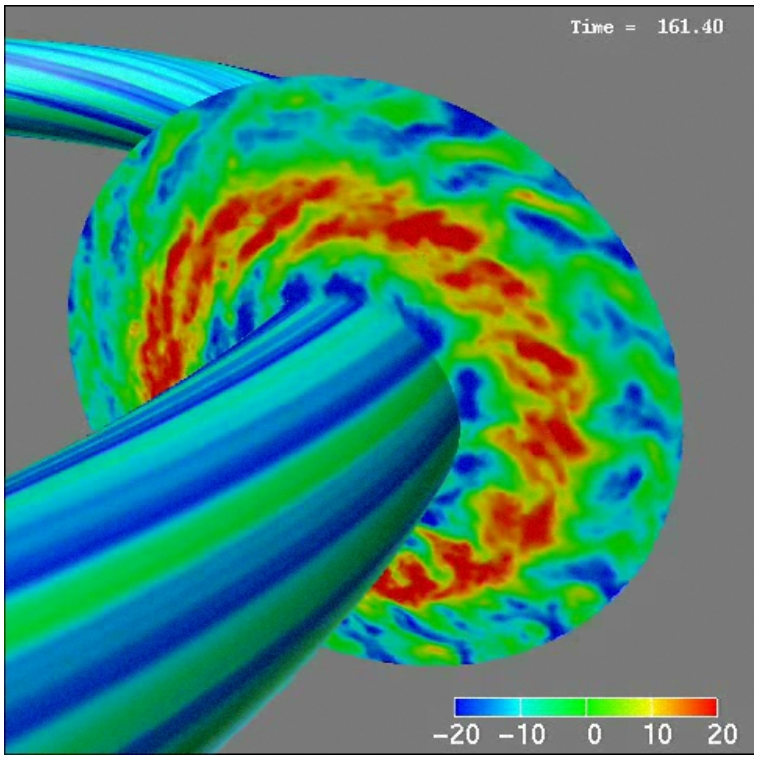

FIGURE 16. ITG simulation from Wakanabe GKV

Balescu version of the Hamaguchi-Horton slab ITG model as an example of a new model that needs numerical solving. Following Balescu [46, p.33] we find that the ITG mode has four partial differential equations,

$$\frac{\partial \delta n_i}{\partial t} = -v_{de}\frac{\partial \delta\phi}{\partial y} - \nabla_\parallel \delta v_\parallel - \frac{c_s^2}{\Omega_i}\left[\delta\phi, \delta n_i\right] \tag{28}$$

$$\frac{\partial}{\partial t}\left(\delta n_i - \rho_s^2\nabla_\perp^2\delta\phi\right) = -v_{de}\frac{\partial}{\partial y}(1-\tau(1+\eta_i)\rho_s^2\nabla_\perp^2)\delta\phi - \nabla_\parallel\delta v_\parallel$$
$$-\frac{c_s^2}{\Omega^i}\left[\delta\phi, (\delta n_i - \rho_s^2\nabla_\perp^2\delta\phi)\right] \tag{29}$$

$$\frac{\partial \delta v_\parallel}{\partial t} = -\frac{1}{m_i n_0}\nabla_\parallel \delta p_i - c_s^2\nabla_\parallel\delta\phi - \frac{c_s^2}{\Omega_i}\left[\delta\phi, \delta v_\parallel\right] \tag{30}$$

$$\frac{\partial \delta p_i}{\partial t} = -v_{de}\tau(1+\eta_i)\frac{\partial\delta\phi}{\partial y} - \Gamma p_{i0}\nabla_\parallel\delta v_\parallel - \frac{c_s^2}{\Omega_i}\left[\delta\phi, \delta p_i\right] \tag{31}$$

where $\tau = T_i/T_e$, $v_{de} = (\rho_s/L_n)c_s$ and Γ is the ion adiabatic gas constant. Each equation has a convective nonlinearity.

Currently there are a number of global and flux-tube codes that simulate the full gyro-kinetic equations for the ITG turbulence Lin et al. [47], Dimits et al. [48], Jenko and Dorland [49]. Here we show the distribution of the electrostatic potential fluctuations in all three dimensions in Fig. 16. In this figure where saturation has occurred, the tendency for the fluctuations to establish a zonal-flow pattern is evident.

6.1. Closure models

When the velocity moments of the original gyrokinetic equation are taken to derive the gyrofluid equations, we need to construct closure models which describe high-order moment variables arising from kinetic effects such as parallel streaming, finite gyroradii, and toroidal magnetic drift. Closure models for these kinetic effects were proposed in a

series of works by Hammett & Perkins [38], Dorland & Hammett [50], and Beer *et. al.* [51]. In these models, high-order moment variables are written in dissipative forms given by linear combination of low-order moment variables so as to reproduce well the linear kinetic dispersion relation. In the Hammett-Perkins model, the parallel heat flux $q_{\|\mathbf{k}}$ with the wave number vector $\mathbf{k}$ is given in terms of the temperature fluctuation $T_{\mathbf{k}}$ as

$$q_{\|\mathbf{k}} = -2\sqrt{\frac{2}{\pi}}\, n_0 v_t\, i\frac{k_\|}{|k_\||} T_{\mathbf{k}}, \tag{32}$$

where $k_\|$ is the wave number in the direction parallel to the magnetic field. The Hammett-Perkins model is successfully applied to calculation of frequencies and growth rates of linear ITG modes while it does not discribe time-reversal symmetric behaviors of the three-mode nonlinear kinetic ITG system [39] which consists of two unstable slab ITG modes and a stable mode representing a quasilinear flattening of the background temperature profile. Mattor & Parker [39] presented a nonlinear closure model and successfully reproduced the solution of the three-mode ITG problem although it cannot be easily extended to turbulent systems with a large number of degrees of freedom.

Realizing that the time-reversal symmetric solution of the three-mode ITG problem can be represented by the superposition of an unstable normal-mode distribution function and its complex conjugate, Sugama, Watanabe & Horton [40] proposed the nondissipative closure model (NCM) which relates the parallel heat flux $q_{\|\mathbf{k}}$ in the linearly unstable wave number region to the temperature fluctuation $T_{\mathbf{k}}$ and the parallel flow $u_{\mathbf{k}}$ in terms of real-valued coefficients,

$$q_{\|\mathbf{k}} = C_{T\mathbf{k}} n_0 v_t T_{\mathbf{k}} + C_{u\mathbf{k}} n_0 T_i u_{\mathbf{k}} \qquad \text{(for linearly unstable modes)}, \tag{33}$$

where the real-valued coefficients $C_{T\mathbf{k}}$ and $C_{u\mathbf{k}}$ are determined by requiring that the kinetic dispersion relation should be derived from the closure relation. The NCM gives the correct relation between $q_{\|\mathbf{k}}$, $T_{\mathbf{k}}$, and $u_{\mathbf{k}}$ both for the unstable normal-mode solution and its complex-conjugate solution as well as for any linear combination of these solutions.

Since the time reversal symmetry of the original collisionless kinetic equation is retained in Eq. (33), the NCM can exactly reproduce the solution of the three-mode ITG problem.

Furthermore, the NCM was used in two-dimensional fluid simulation of the strong turbulence driven the slab ITG modes and its validity for quantitative prediction of the anomalous ion thermal transport in the slab ITG turbulence was confirmed by comparison to collisionless kinetic simulation results as shown in Fig. 17 [52].

We should note that the NCM can be applicable only to linearly unstable modes and that the Hammett-Perkins-type dissipative closure model was still used for linearly stable modes even for the NCM fluid simulation.

In the slab ITG turbulence shown in Fig. 17, the zonal-flow component was not included whereas only quiet steady states with turbulence transport suppressed by large zonal-flow generation were obtained by both of our kinetic and fluid simulations when including the zonal flow component [53].

In toroidal configurations, zonal-flow generation is weaker than in slab cases although zonal flows are still an important factor to regulate turbulent transport and a wrong description of zonal flows was once suspected by Rosenbluth & Hinton [54] as a cause of difference between gyrokinetic and gyrofluid simulation results of toroidal ITG turbulence.

Improved closure models, which give residual zonal flows predicted by Rosenbluth & Hinton, were proposed by Beer & Hammett [55] and recently by Sugama, Watanabe, & Horton [56].

7. CONCLUSIONS

The basic physical mechanisms of drift-wave instabilities and the associated plasma transport are described in detail. Drift waves develop into a mixture of wave turbulence and coherent structures with details of the mixture depending on the driving forces ∇n_e, ∇T_e and ∇T_i and the amount of magnetic shear and background velocity shear in the system. The mixture of zonal flows, waves and vortices has certain similarities to the Rossby waves in planetary atmospheres and the equatorial-to-polar temperature gradient driven turbulent heat. The principal difference is in the replacement of the gravitational force on planets with a electric force from charge separation in the curved magnetic fields.

The free energy sources created by the radial gradients of the plasma density and the temperature are useful to characterize the strength of the drift wave turbulence. We have suggested that real time diagnostic signals from microwave interferometers and Thompson scattering data can be used to compute the thermodynamic formulas for the upper bounds of the turbulence given in Sec.2 for the density and temperature fluctuations. The derivations of the

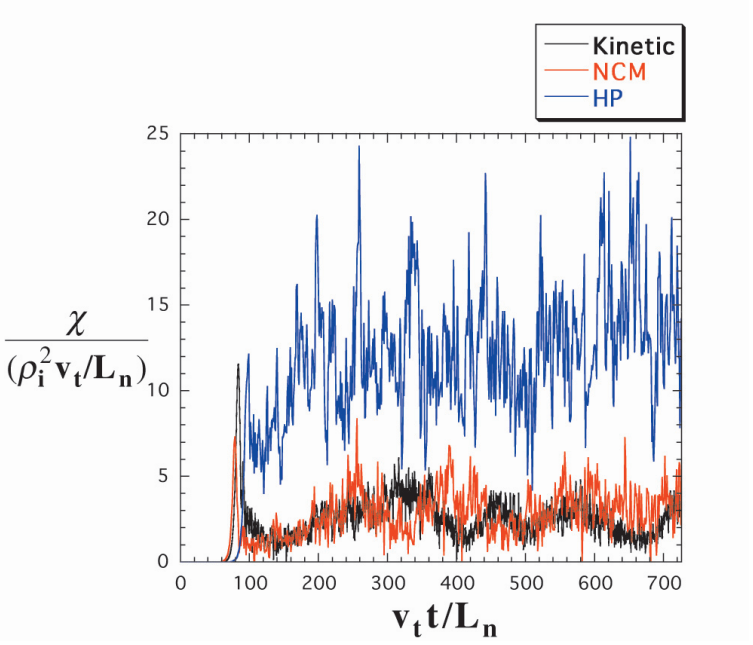

FIGURE 17. Normalized turbulent ion heat diffusivity $\chi/(\rho_i^2 v_t/L_n)$ as a function of normalized time $v_t t/L_n$ obtained by the two-dimensional slab ITG turbulence simulation [52]. Black, red, and blue lines correspond to results from the kinetic simulation, the fluid simulation using the NCM, and that using the Hammett-Perkins (HP) model, respectively.

free energy formulas treat the plasma as an ideal gas with a compressibility gas constant, $\Gamma = (d+2)/d$, where d is the number of degrees of freedom associated with the type of instability under investigation. The Carnot-cycle description of the auxiliary heated plasma is particularly relevant and was used in Horton et al. [57] for the electron temperature profiles in Tore Supra and is being used for real-time data in NSTX.

The structure of the drift wave eigen-modes in the double-periodic toroidal geometry is described after a brief review of the early experiments on drift waves in steady state cylindrical Q-machines. The recent experiments in the Columbia Linear Machine [17] devoted to the ion temperature gradient (ITG) mode and the 6-channel CO_2 laser scattering experiments in TEXT [15] clearly show the role of the hybrid ITG mode and trapped electron mode TEM.

The ITG mode has become the standard model for describing ion transport in basically all toroidal experiments with strong ion temperature gradients. The basic toroidal mechanism and nonlinear models are given in Horton et al. [43]. Nowadays large-scale Tera-flop computers commonly compute the ITG turbulence from direct numerical solutions of the gyrokinetic-Vlasov-Poisson system and as an example the state of the turbulence is shown in section 6 from the NIFS GKV simulation. The standard article on the comparison of direct numerical simulation for the ITG turbulence is Dimits et al. [48]. Review of the state of the numerical simulations of the ETG turbulence is Nevins et al. [58]. The electron turbulent transport is more demanding to compute but shows very large enhancements over the quasi-linear fluxes due to the formation of extended radial structures with correlation lengths, $\ell_c \gg \rho_e$, and the structures are insensitive to the radial electric-field shear but do depend sensitively on the magnetic-shear profile.

The empirical energy confinement scaling laws for both helical system [8] and tokamaks [6, 7] follow the drift-wave formulas and simulations to within the accuracy of the experimental data. Some of the more detailed comparisons of theoretical models [59, 60, 61, 62] with tokamak databases are referenced but a detailed discussion is beyond the scope of this chapter.

REFERENCES

1. W. Horton, and L. E. Reichl, editors, *Statistical Physics and Chaos in Fusion Plasmas*, John Wiley & Sons, New York, 1984.
2. S. Benkadda, Y. Elskens, and F. Doveil, editors, *Transport, Chaos and Plasma Physics:Institut Mediterraneen De Technologie, Marseille, France 10-21 July, 1995*, Advanced Series in Nonlinear Dynamics, World Scientific Pub Co Inc, 1995.
3. W. Horton, and Y. Ichikawa, *Chaos and Structures in Nonlinear Plasmas*, World Scientific, 1996.

4. G. T. Hoang, W. Horton, C. Bourdelle, B. Hu, X.Garbet, and M. Ottaviani, *Phys. Plasmas* **10**, 405–412 (2003).
5. I. H. mode Database Working Group, *Nucl. Fusion* **34**, 131–167 (1994).
6. S. Kaye, M. Greenwald, U. Stroth, O. Kardaun, A. Kus, D. Schissel, J. DeBoo, G. Bracco, K. Thomsen, J. Cordey, Y. Miura, T. Matsuda, H. Tamai, T. Takizuda, T. Hirayama, H. Kikuchi, O. Naito, A. Chudnovskij, J. Ongena, and G. Hoang, *Nucl. Fusion* **32**, 1303–1328 (1997).
7. I. P. E. Group, *Nucl. Fusion* **39**, 2175 (1999).
8. H. Yamada, J. H. Harris, A. Dinkalge, E. Ascasibar, F. Sano, S. Okamura, J. Talmadge, U. Stroth, A. Kus, S. Murakami, M. Yokoyama, C. D. Beidler, V. Tribaldos, K. Y. Wantanabe, and Y. Suzuki, *Nucl. Fusion* **45**, 1684–1693 (2004).
9. E. of 'Progress of ITER Physics Basis', *Nucl. Fusion* **47**, S1–S17 (2007).
10. B. Kadomtsev, and O. Pogutse, "Turbulence in Toroidal systems," in *Reviews of Plasma Physics, Volume 5*, edited by A. Leontovich, 1970, pp. 249–400.
11. D. Bohm, E. H. S. Burhop, and H. S. W. Massey, "The use of probes for plasma exploration in strong magnetic fields," in *The characteristics of electrical discharges in magnetic field*, edited by A. Guthrie, and R. K. Wakerling, New York, McGraw-Hill, 1949.
12. W. Horton, B. G. Hong, and W. M. Tang, *Phys. Fluids* **31**, 2971 (1988).
13. H. W. Hendel, T. K. Chu, and P. A. Politzer, *Phys. Fluids* **11**, 2424–2439 (1968).
14. F. F. Chen, *Introduction to plasma physics and controlled fusion*, Plenum Press, New York, 1974.
15. D. L. Brower, W. A. Peebles, S. K. Kim, N. C. Luhmann, W. M. Tang, and P. E. Phillips, *Phys. Rev. Lett.* **59**, 48–51 (1987).
16. E. Mazzucato, *Phys. Rev. Lett.* **36**, 792–794 (1976).
17. A. K. Sen, J. Chen, and M. Mauel, *Phys. Rev. Lett.* **66**, 429–432 (1991).
18. T. Cho, J. Kohagura, T. Numakura, M. Hirata, H. Higaki, H. Hojo, M. Ichimura, O. Watanabe, M. Yoshikawa, A. Kojima, Y. Miyake, Y. Miyata, K. Shimizu, Y. Tomii, M. Yoshida, K. Sakamoto, T. Imai, V. P. Pastukhov, S. Miyoshi, and G. . Group, *Phys. Rev. Lett.* **97**, 055001 (2006).
19. H. Hojo, *Jpn. J. Appl. Phys.* **34**, 6501 (1995).
20. S. Hamaguchi, and W. Horton, *Phys. Fluids B* **2**, 1833–1851 (1990).
21. S. Hamaguchi, and W. Horton, *Phys. Fluids B* **4**, 319–328 (1991).
22. S. Hamaguchi, and W. Horton, *Plasma Phys. Contr. Fusion* **35**, 203–233 (1992).
23. Y. Kishimoto, T. Tajima, W. Horton, M. J. LeBrun, and J. Y. Kim, *Phys. Plasmas* **3**, 1289–1307 (1996).
24. P. Terry, *Rev. Mod. Phys.* **72**, 109–165 (2000).
25. D. Newman, B. Carreras, D. Lopez-Bruna, P. Diamond, and V. Lebedev, *Phys. Plasmas* **05**, 938 (1998).
26. H. Biglari, P. H. Diamond, and P. W. Terry, *Phys. Rev. Lett.* **60**, 200–203 (1988).
27. J. Q. Dong, W. Horton, and J. Y. Kim, *Phys. Plasmas* **4**, 1867–1876 (1992).
28. K. Itoh, and S.-I. Itoh, *Plasma Phys. Contr. Fusion* **38**, 1–49 (1996).
29. P. H. Diamond, I. S-I, K. Itoh, and T. S. Hahm, *Plasma Phys. Contr. Fusion* **47**, R35–R161 (2005).
30. J. Perez, W. Horton, K. Gentle, W. Rowan, K. Lee, and R. Dahlburg, *Phys. Plasmas* **13**, 2101–2110 (2006).
31. T. Cho, J. Kohagura, M. Hirata, T. Numakura, H. Higaki, H. Hojo, M. Ichimura, K. Ishii, K. M. Islam, A. Itakura, I. Katanuma, Y. Nakashima, T. Saito, Y. Tatematsu, M. Yoshikawa, Y. Takemura, A. Kojima, T. Kobayashi, Y. Yamaguchi, Y. Miyata, N. Yokoyama, Y. Tomii, Y. Miyake, S. Kiminami, K. Shimizu, Y. Kubota, H. Saimaru, Y. Higashizono, A. Mase, Y. Yasaka, K. Ogura, K. Sakamoto, M. Yoshida, V. P. Pastukhov, T. Imai, S. Miyoshi, and G. . Group, *Nucl. Fusion* **45**, 1650–1657 (2005).
32. J.-H. Kim, J. C. Perez, W. Horton, G. Chagelishvili, R. G. Chanishvili, J. G. Lominadze, and J. C. Bowman, *Phys. Plasmas* **13**, 2304 (2006).
33. T. H. Stix, *Waves in Plasmas*, Springer, 1992.
34. R. E. Slusher, and C. M. Surko, *Phys. Rev. Lett.* **40**, 400–403 (1976).
35. W. Horton, *Phys. Rev. Lett.* **37**, 1269–1272 (1976).
36. X. L. Zou, L. Colas, M. Paume, J. M. Chareau, L. Laurent, P. Devynck, and D. Gresillon, *Phys. Rev. Lett.* **75**, 1090–1093 (1995).
37. L. Colas, X. L. Zou, M. Paume, J. M. Chareau, L. Guiziou, G. T. Hoang, Y. Michelot, and D. Gresillon, *Nucl. Fusion* **38**, 903–918 (1998).
38. G. W. Hammett, and F. W. Perkins, *Phys. Rev. Lett.* **64**, 3019–3022 (1990).
39. N. Mattor, and S. E. Parker, *Phys. Rev. Lett.* **79**, 3419–3422 (1997).
40. H. Sugama, T. H. Watanabe, and W. Horton, *Phys. Fluids* **8**, 26172628 (2001).
41. W. Horton, R. Estes, and D. Biskamp, *Plasma Physics* **22**, 663–678 (1980).
42. A. M. Dimits, J. F. Drake, P. N. Guzdar, and A. B. Hassam, *Phys. Plasmas* **3**, 620–626 (1991).
43. W. Horton, D. I. Choi, and W. M. Tang, *Phys. Fluids* **24**, 1077–1085 (1981).
44. R. E. Waltz, G. D. Kerbel, and J. Milovich, *Phys. Plasmas* **1**, 2229–2244 (1994).
45. M. A. Beer, and G. W. Hammett, *Phys. Plasmas* **3**, 4046–4064 (1996).
46. R. Balescu, *Aspects of anomalous transport in plasmas*, Series in Plasma Physics, Institute of Physics Publishing, 2005.
47. Z. Lin, T. S. Hahm, W. W. Lee, W. M. Tang, and R. B. White, *Science* **281**, 1835–1837 (1998).
48. A. M. Dimits, G.Bateman, M. A. Beer, B. I. Cohen, W. Dorland, G. W. Hammett, C. Kim, J. E. Kinsey, M. Kotschenreuther, A. H. Kritz, L. L. Lao, J. Mandrekas, W. M. Nevins, S. E. Parker, A. J. Redd, D. E. Shumaker, R. Sydora, and J. Weiland, *Phys. Plasmas* **7**, 969–983 (2000).
49. F. Jenko, and W. Dorland, *PPCF* **43**, A141–A150 (2001).

50. W. Dorland, and G. W. Hammett, *Phys. Fluids B* **5**, 812–835 (1993).
51. M. A. Beer, G. W. Hammett, G. Rewoldt, E. J. Synakowski, and M. C. Zarnstorff, *Phys. Plasmas* **4**, 1792–1799 (1997).
52. H. Sugama, T.-H. Watanabe, and W. Horton, *Phys. Plasmas* **10**, 726–736 (2003).
53. T. H. Watanabe, and H. Sugama, *Phys. Plasmas* **9**, 3659–3662 (2002).
54. M. N. Rosenbluth, and F. L. Hinton, *Phys. Rev. Lett.* **80**, 724 – 727 (1998).
55. M. A. Beer, and G. W. Hammett, "," in *Proceedings of the Joint Varenna-Lausanne International Workshop on Theory of Fusion Plasmas, Varenna, 1998*, edited by J. W. Connor, E. Sindoni, and J. Vaclavik, Bologna, Societa Italiana de Fisca, 1999.
56. H. Sugama, T.-H. Watanabe, and W. Horton, *Phys. Plasmas* **14**, 022502 (2007).
57. W. Horton, H. V. Wong, P. J. Morrison, A. Wurm, J. H. Kim, J. C. Perez, J. Pratt, G. T. Hoang, B. P. LeBlanc, and R. Ball, *Nuclear Fusion* **45** (2005).
58. W. M. Nevins, J. Candy, S. Cowley, T. Dannert, A. Dimits, W. Dorland, C. Estrada-Milla, G. W. Hammett, F. Jenko, M. J. Pueschel, and D. E. Shumaker, *Phys. Plasmas* **13**, 122306 (2006).
59. J. E. Kinsey, G. Bateman, A. H. Kritz, and A. Redd, *Phys. Plasmas* **3**, 561–570 (1996).
60. J. E. Kinsey, and G. Bateman, *Phys. Plasmas* **3**, 3344–3357 (1996).
61. A. J. Redd, A. H. Kritz, G. Bateman, and W. Horton, *Phys. Plasmas* **5**, 1369–1379 (1998).
62. G. Bateman, A. H. Kritz, J. E. Kinsey, and A. J. Redd, *Phys. Plasmas* **5**, 2355–2362 (1998).